Avoiding abnormal grain growth in thick 7XXX aluminium alloy friction stir welds during T6 post heat treatments

Matthieu B. Lezaack[a], Aude Simar[a]

[a] Institute of Mechanics, Materials and Civil Engineering, Université catholique de Louvain, B-1348 Louvain-la-Neuve, Belgium

Abstract

Friction stir welding (FSW) is becoming an essential welding technique in the aerospace industry. However, friction stir welds are usually weaker than the parent material. The dissipated heat causes a softening of the 7XXX series aluminium alloys. Post-welding heat treatments are used to restore the highest strength after welding. The reference treatment is composed of two-steps heating: a solution heat treatment typically at 470°C for 30 minutes, quench in water followed by artificial aging 120°C for 24 hours. These treatments are responsible for very significant grain coarsening in the weld nugget zone known as secondary recrystallization, sometimes leading to abnormal grain growth (AGG). This is particularly true for thick plates. This secondary recrystallization phenomenon is detrimental for tensile performances. A detailed analysis of the conditions leading to secondary recrystallization during post-welding heat treatments is provided. A procedure to avoid secondary recrystallization in FSWed joints is then highlighted. Thermal cycles during welding are controlled by welding on a low thermal conductivity backing plate (i.e. stainless steel) which avoids very fine grains in the bottom of the weld nugget. This new procedure opens the path to excellent welds presenting at least the strength and ductility of the T6 base material.

Key words

Friction Stir Welding, 7XXX Aluminium Alloys, Abnormal Grain Growth, Solution Heat Treatments, Precipitation, Mechanical Properties

Highlights

- Influence of backing plate material on FSW microstructure and mechanical properties
- Avoiding grain growth during solution heat treatment of friction stir welds
- Strength and ductility similar to the T6 state of 7XXX aluminium plate obtained after FSW and heat treatments

1. Introduction

1.1. High strength 7XXX aluminium alloys and their fusion welding

Aluminium alloys of the 7XXX series were developed aiming at both high strength and high toughness. 7XXX series reach the highest yield stress compared to all other industrial aluminium alloys by the formation of heat sensitive $MgZn_2$ precipitates, also identified as the semi-coherent η' phase [1]. Depending on the processing routes, size and distribution of precipitates can be tuned to the hardest temper: the T6 state. In T6 conditions, the yield strength overtakes 500 MPa for most 7XXX alloys [2][3].

The aerospace industry has successfully integrated the 7XXX high strength alloys in aircraft design. However, 7XXX series are known to be hard to weld by conventional fusion techniques due to their susceptibility to hot cracking [4]. Modifying the alloy composition is the most classical route to adapt MIG technique to 7XXX sheets, e.g. by adding Scandium [5]. However, the mechanical properties of these MIG-welding alloys are not reaching the requirements for current high-end applications [5].

1.2. Friction stir welding for 7xxx series Al alloys

Friction stir welding is a promising solid-state process introduced by the Welding Institute (TWI), United Kingdom, in 1991 [6] and reviewed by Ref. [4][7][8][9] that can produce sound 7XXX series welds. FSW avoids detrimental mechanical performances associated to solidification defects. Intense plastic deformation and material flow between parts to be joined is leading to high efficiency welds [4][7]. FSW is known to generate a heterogeneous microstructure [10][11]. The stirring tool leads to dynamic recrystallization of the highly deformed material, achieving significant grain size refinement in the nugget zone (NZ). Feng *et al.* [12] suggested that Cr-rich E phase dispersoids ($Al_{18}Cr_2Mg_3$ according to Aoba *et al.* [1]) are pinning the dislocations and grain boundaries, limiting the grain growth during FSW in 7XXX series alloys. Beside the NZ, two thermo-mechanically affected zones (TMAZ) are characterized by a heat affected microstructure that suffers plastic deformation during FSW and subsequent recovery of the microstructure [10]. These TMAZ are themselves surrounded by two heat affected zones (HAZ), showing limited macroscopic deformation [10].

Welding parameters can enhance microstructural heterogeneities for some advancing and rotating speeds, keeping tool geometry unchanged. It was noticed by Mishra *et al.* that temperature affects NZ microstructure [4]. Cooler conditions, corresponding to lower rotational speed and higher advancing speed, are limiting the grain growth after dynamic recrystallization in the NZ [4].

During welding, thermal gradient is usually reported because tool shoulder generates most of the heat [4]. Higher temperatures are favouring grain boundary mobility in top regions, generating coarser grains near tool shoulder according to Huang *et al.* [13]. Lower temperature is reached in bottom of the weld because of the backing plate heat absorption [4]. Faster cooling rates in the backing plate region is limiting grain growth [4].

The main limitation of FSW on 7XXX series is related to the softening when welded in T6 or T7 states. Heat is dissolving η' and coarsening the incoherent η precipitates. Feng *et al.* [12] and Martinez *et al.* [14] showed the dissolution and re-precipitation of hardening elements by DSC measurements in the 7XXX alloys subjected to FSW. In particular, none of the pre-existing η' precipitates survive the FSW heat cycle in the NZ (i.e. full precipitate dissolution occurs), leading to significant softening.

1.3. Softening of 7XXX FSWed material

FSW material softening is related to precipitation coarsening. Temperature, dislocations and grain boundaries are affecting the as-welded precipitation state. During FSW, alloying elements are dissolved before NZ dynamic recrystallization according to Su *et al.* and Martinez *et al.* [10][14]. During subsequent cooling, coarse precipitates nucleates preferentially on grain boundaries. Su *et al.* [10] showed that most of the grains in NZ have high angle grain boundaries misorientation, i.e. greater than 15°. Nucleation and coarsening of precipitates is easier on high angle misorientation grain boundaries. On the contrary, un-recrystallized grains do not favour coarse precipitation as they are forming low angle grain boundaries within sub-grain structures.

According to Mishra *et al.* and Su *et al.*, dislocation density is possibly high in some NZ region, at least in a many NZ grains [4][10]. Su *et al.* obtained ultra-fine grains, showing lower dislocation density in the bottom part of the NZ. The explanation stands that the coarser grains in the top part of the NZ are further deformed after dynamic recrystallization, leading to higher dislocation density compared to the bottom regions [10]. The high dislocation density zones favours elements diffusion at high temperature by pipe diffusion mechanisms according to Ma *et al* [15]. During cooling, the precipitates nucleate and subsequently exhibit a faster growth due to the higher solute elements mobility, as described by Su *et al.* on 7050 alloy [10].

An attempt to limit softening during FSW of 7XXX alloys was proposed by controlling temperature and heat generated during the FSW process in Martinez *et al.* work [14]. Martinez was playing on tool geometry and FSW parameters. Similarly, Zhang *et al.* performed some extensive parametric studies, varying the rotational and advancing speeds, in order to avoid excessive heating and the resulting alloy softening [16]. Zhang *et al* showed that as-FSWed samples can lead to 75% strength efficiency welds. [16]. Applying cold welding conditions is a necessity (low rotational and high advancing speeds), while all hot conditions (high rotational and low advancing speeds) are associated to dramatic decrease in strength and ductility. To reach cold welding conditions, refrigerated anvils can be used, as investigated by Liu *et al.* [17]. However, the yield stress of cold welds is still reduced compared to the strongest T6 state.

1.4. High strength 7XXX welds

In order to recover full strength (T6) 7XXX welded alloys, post-weld heat treatments were investigated and control the hardening precipitation after FSW.

Sivaraj *et al.* [18] and Hu *et al.* [19] applied 2-step T6 heat treatment on 7075 and 2024 welded alloys respectively. After conventional FSW, high temperature solution heat treatments (SHT) dissolve the hardening precipitates throughout the entire welded component. A quench is then performed and the material can subsequently be artificially aged at lower temperature to re-generate the fine T6 temper precipitation. Using appropriate SHT conditions on Cu-rich 2XXX alloys, excellent welds were obtained reaching the strength level of the T6 base material [19].

However, for 7XXX series, a higher SHT temperature is needed. NZ grain growth by secondary recrystallization and even abnormal grain growth (AGG) was reported by Charit *et al.* [20], Hassan *et al.* [21] and Sajadifar *et al.* [22] on 7XXX alloys. AGG affects mechanical performance of several alloys (2XXX, 5XXX, 6XXX) and should be as limited as possible to ensure good ductility [20][21][22][23][24]. In the worst cases of secondary recrystallization, mm-scale grains were measured by Hassan *et al.* [21].

If SHT conditions leads to AGG, a coarse columnar microstructure is generated in part of the NZ [21]. The weld elongation under transverse tension decreases dramatically, as shown by Sajadifar *et al.* [22]. The T6 heat treated welds reach almost 100% strength efficiency but only 15% ductility efficiency in comparison with the T6 rolled material [22]. As reported by Ludtka *et al.*, the columnar microstructure is acting as a preferential path for crack propagation due to the inter-granular damage nucleation, typical of the 7XXX series alloys [3].

1.5. Secondary recrystallization in aluminium alloys

The secondary recrystallization during SHT is thus detrimental for welds mechanical properties. Influencing parameters are reviewed in next paragraphs.

Secondary recrystallization (eventually in AGG mode) phenomenon is not limited to FSW material. Sun *et al.* are demonstrating that secondary recrystallization also occurs on extruded material [25]. Extrusion is generating a composite microstructure with recrystallized bands alternating with deformed and restored grains. Extruded fine grains are sensitive to recrystallization and coarsening during post-extrusion SHT. Sun *et al.* noticed that secondary recrystallization is taking place in a very short duration [25]. Indeed, 5 minutes SHT on a 7050 extruded sample is already sufficient to generate AGG [25].

On friction stir welds, Hassan *et al.* showed that recrystallization depends on SHT temperature [21]. Final grain size and recrystallized proportion on FS welds are also dependant of the SHT heating rate on a 7010 alloy [21]. The most influent parameter on recrystallization final aspect and proportions is the FSW processing conditions. Hot FSW conditions (high rotational and low advancing speeds) is leading to more stable NZ microstructure, limiting the recrystallized area after SHT [20][21].

1.6. Microstructural sources of secondary recrystallization

The various microstructural features in the NZ that may influence secondary recrystallization will now be detailed: dispersoids and precipitates, dislocation density, prior grain size and texture.

Firstly, Liu *et al*. relate (abnormal) grain growth to dissolution of hardening pinning second phases in 2XXX Al series during SHT [17]. In 7XXX alloys, Hassan *et al*. relate dispersoids and coarse precipitates to recrystallization mechanisms [21]. Planar fronts of secondary recrystallization are forming following the dissolution of hardening precipitates, leading to mm-scale grains [21]. Indeed, grain boundaries are pinned by hardening precipitates until their dissolution [17]. However, dispersoids density is not supposed to be sufficient to prevent grain growth on 7010 alloy according to Hassan *et al.* [21].

Second, dislocation density in NZ seems to fluctuate in literature results [4][10][26][27]. At that stage, the dislocation density may influence grain growth during secondary recrystallization. In order to confirm or infirm the relation between dislocations and recrystallization by normal or abnormal grain growth under SHT, Charit *et al*. have shown that residual strain related to dislocation density is not affecting the AGG in 7075 alloy [20]. Dislocation density is not the only driving force for AGG inside FSW nuggets.

Thirdly, initial grain size (i.e. before the SHT) seems to have a first order effect on recrystallization during SHT. Finer grains regions are more prone to recrystallization according to Hassan *et al*. [21]. For extruded 7050 alloy, Sun *et al.* have shown that coarser grains act as a barrier to secondary recrystallization of small grains [25]. Hu *et al*. studied the grain size along top – middle – bottom locations of friction stir welds in 2024 alloy [19]. They tuned welding parameters to limit recrystallization during SHT. Using higher heat input during FSW; grain size is coarser in NZ and more homogeneous throughout the weld thickness. These specific conditions are leading to welds more resistant to (abnormal) grain growth during subsequent SHT.

The final microstructural feature playing a role on secondary recrystallization is grain texture and grain boundaries orientations. Indeed, grain boundary misorientation has an influence on grain boundary mobility. Higher mobility (associated to lower misorientation) is corresponding to higher grain growth rates according to Humphreys *et al.* [28]. Charit *et al*. have reported that texture heterogeneities due to the FSW plastic deformation in 7075 alloy have a direct impact on secondary recrystallization [20]. In extruded 7050 alloy, Sun *et al.* revealed that AGG depends on texture [25]. For a deeper analysis of these heterogeneities, Mironov *et al*. investigated grain texture orientation in the NZ [29][28]. The authors noticed that as-FSWed joints do not have random grain boundary angle distribution: preferential orientations are observable depending on shearing of the material in the TMAZ-NZ zones (large scale compared to grain size). During the SHT, initial grains orientation enforce the recrystallization of the material, influencing the AGG texture. Xu *et al.* identified a stronger texture on pole figures when scanning from top to bottom of the FS welds. This may be explained by the lower temperature and limited grain growth during dynamic recrystallization [11]. On the other hand, Mironov *et al.* performed full weld section EBSD (electron backscattered diffraction) mapping, proving that the nugget zone texture is influenced by the shearing direction during stirring [29]. Thus, the cross-section texture is varying significantly from one nugget band to the next. Furthermore, Mironov *et al.* proved that the AGG is not leading to random orientations. Indeed, the coarse recrystallized grains shows a 30° rotation around the (111) crystallographic orientation in comparison to the as-welded microstructure [29].

1.7. Preventing secondary recrystallization in 7XXX alloys

In order to prevent recrystallization and grain growth, several methodologies were investigated.

First, pre-welding heat treatments were investigated to play on the dispersoid particles size. AGG resistant methods were developed by Ehrstrom *et al* [30]. Cr-rich and/or Zr-rich dispersoids are coarsened by high temperature treatments prior to FSW. Indeed, FSW is not dissolving these dispersoids [10]. With this processing route, dispersoids pin grain boundaries, leading to smaller recrystallized grains during SHT. However, the obtained microstructure is still significantly coarser than initial NZ as the recrystallization is not fully inhibited.

A second method is related to FSW stirring optimization. Charit *et al*. suggest that tool design is a solution for recrystallization resistant welds on 7XXX series [20]. It was suggested that grain size and plastic flow can be homogenized by adapting tool geometry. A more homogeneous and stable microstructure would then be more resistant to secondary recrystallization.

Beside tool optimization, FSW parameters (advancing and rotating speeds) may be tuned in order to prevent grain coarsening (see supplementary data, Figure S1). However, this option was not highly successful as most of the configurations led to AGG. A classification of the heat-treated samples shows that the grain coarsening and AGG are related to the amount of heat generated during FSW. According to Charit *et al.*, Hassan *et al.* and Hu *et al.*, hot welds (low advancing speed and/or high rotational speed) are more resistant to grain recrystallization in post-FSW heat treatments [19][20][21].

Finally, some exotic FSW setups were developed, aiming at limiting recrystallization. As grain coarsening (eventually in AGG mode) occurs generally in the bottom part of the welds, Huang *et al*. investigated self-supporting FSW tool (double shoulders) on 6082 alloy material

[13]. The absence of backing plate leads finally to the conclusion that secondary recrystallization is unfortunately still occurring near the top or bottom surface. In these air-cooled welds, the centre of the NZ is more stable. High heat absorption of the backing plate is not the only parameter leading to recrystallization. However, compared to the results of Charit *et al*., where a significant amount of the NZ had recrystallized into coarse grains, only limited amount of grains are coarsening in the NZ of self-supported FSW joints [20]. Lower heat dissipation impacts positively the recrystallized area, as will also be shown in the present work.

Overlapping friction stir processing (O-FSP) has also been attempted by Jana *et al*. [31] with an aim to restrain secondary recrystallization. Overlapping is performed on F357 alloy (Al-Si-Mg) in order to reach higher homogeneity in refined over-lapped NZ. However, secondary recrystallization could not be avoided by O-FSP. The conclusions are demonstrating a higher grain stability for higher rotational speeds and overlaps compared to one-pass identical conditions.

1.8. Objectives of this work

The present work thus presents a methodology to understand, control and totally inhibit secondary recrystallization during post-SHT of 7XXX FSW joints, described in section 2. In this experimental work, bead-on-plate FSW joints will generate different microstructures, playing on FSW thermal cycles. Some of the generated samples are sensitive to secondary recrystallization during high temperature post-treatments, as observed in 7XXX literature and described in section 3 [20][21]. Section 4 will discuss the path leading to a fine FSW microstructure after a T6 post treatment without coarsening the initial NZ grains. Wide experimental campaigns could be avoided by playing only on cooling rates of the welds. Expanding obtained results allows to get rid of secondary recrystallization and AGG in 7XXX FSWed alloys. Producing high strength welds associated to a fine microstructure are promising for industrial applications.

2. Experimental procedure

2.1. Material

The 7475 aluminium alloy in T7351 state was selected in this study. The as-received material is a 12 mm thick rolled plate. The alloy's composition is identified by inductively coupled plasma optical emission spectroscopy (ICP).

2.2. Material processing and in-situ measurements

Bead-on-plate welds are achieved using a dedicated FSW machine (FSW-LM-AM-16-2D, Tra-C industries). FSW is performed using threaded-tri-flat conical pin tool made of H13 tool steel. The pin is 10 mm in length, 6 mm in reduced diameter, 10 mm in root diameter. The tool shoulder is 22 mm in diameter. The excessive 2 mm in plate thickness compared to tool pin are used to machine grooves for thermocouples insertion (see Figure 1).

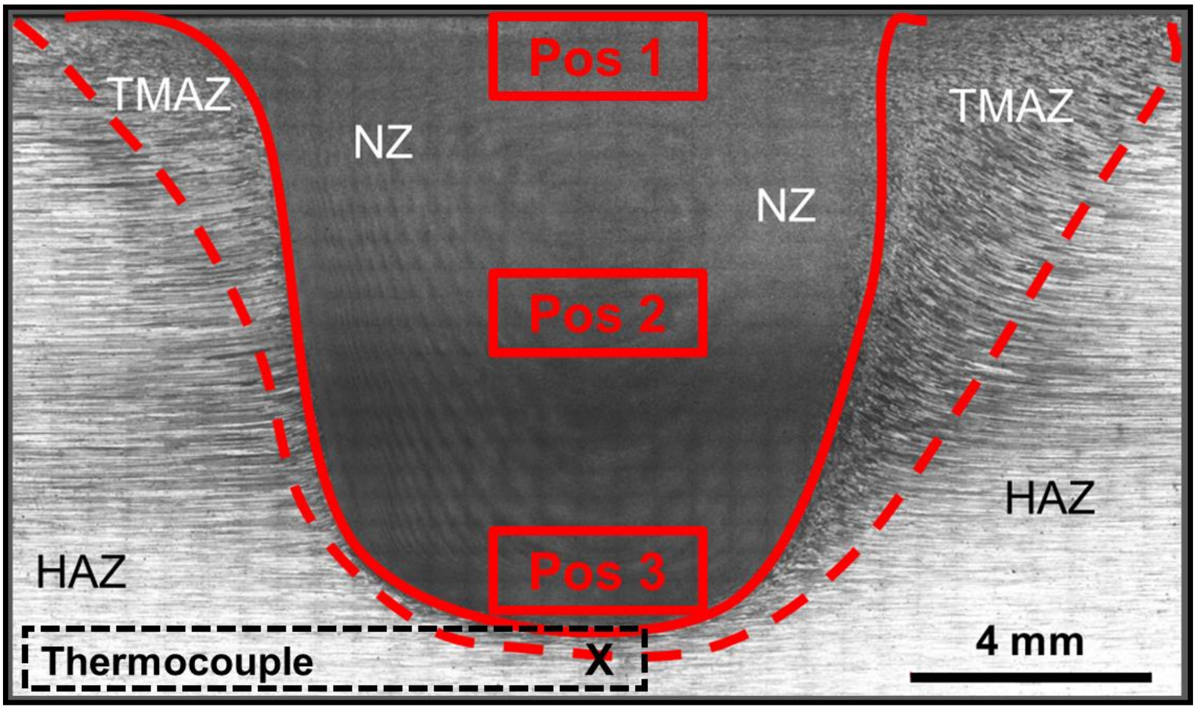

Figure 1: FSWed 7475 sample cross-section, microstructural zones identified (NZ, TMAZ, HAZ); Thermocouple positioning indicated by 'X'. Investigated microstructures are identified as Pos 1 for top region of the NZ, Pos 2 for the middle of NZ and Pos 3 for the bottom part of NZ.

Concerning the FSW machine setup, a rectangular (400 mm x 200 mm) 6 mm thick backing plate under the aluminium samples may be exchanged. Copper, steel and stainless steel backing plates are successively used. Thermal conductivity of these materials are provided in Table 1.

BP:	**Copper**	**Steel**	**Stainless steel**
Thermal conductivity	360 W/(mK)	35-50 W/(mK)	15-20 W/(mK)
Torque measured during FSW	93.0 ± 1.5 Nm	87.6 ± 3.0 Nm	77.9 ± 4.4 Nm

Table 1: Thermal conductivity of the backing plate materials on the range 25°C to 325°C [32], [33] and [34]. Recorded mean torque during FSW, 3 measurements per condition.

Welding parameters were based on literature work [10][18]. After a minor optimisation around these literature parameters to reach sound welds, the parameters were fixed in the present study at an advancing speed equal to 100 mm/min and a rotational speed equal to 300 RPM. FSW is performed in vertical force control (instead of position control), maintaining a constant 15.5 kN vertical load during stirring.

Torque is measured during welding. The torque in the steady state regime is averaged for the three samples produced for each backing plate condition. Values are displayed in Table 1.

Temperature measurements were performed during FSW. K-type thermocouples were inserted in grooves below the stirring tool path in order to record the temperature profile of the bottom region, as described on Figure 1.

Solution heat treatments (SHT) are applied in an air furnace (Nabertherm 1100) to FSWed samples. The reference SHT for this work is 470 ± 5°C for 30 minutes [2][21]. Other combinations are explored in this work, as classified in Table 2. Water quenching is performed right after SHT. The quenched material is then naturally aged at room temperature for at least 14 days. Artificial aging at 120°C for 24 hours results in the hardest T6 state.

Trial ID	Temperature of SHT	SHT duration
1	450°C	5 min
2		30 min
3		120 min
4	470°C	5 min
5		30 min
6		120 min
7	500°C	5 min
8		30 min
9		120 min
	Temperature of SHT	**Heating rate**
10	470°C	3.25°C/h

Table 2: All solution heat treatments (SHT) investigated in this study providing their solution temperature and duration.

2.3. Microstructure and mechanical characterization

Polishing the sample with standard procedures, iron-rich impurities and porosities are contrasting with the aluminium matrix. The grains are revealed using Keller's reagent (as described by Zhang *et al.* [16]). Imaging is achieved by optical Olympus microscope, allowing the full-weld overview. Grains coarser than 100 µm are then easily identified.

Polished samples without chemical etching are characterized using a Field Emission Gun Scanning Electron Microscope (FEG-SEM) Ultra 55. The SEM is used to analyse locally the fine microstructure, from top to bottom of the weld section. Images are taken at three different positions along the weld centreline as described in Figure 1. Back-scattered electron detector is used under 10keV working tension.

Optical and SEM images are analysed using thresholding techniques. Fine FSWed grains are characterized using SEM images, prior to post-weld SHT. Distributions of sizes for grains and for coarse precipitates is recorded according to the position into the weld nugget. At least 1000 grains are counted for each NZ level grain measurement, while at least 2500 coarse precipitates are registered during the image analysis.

Electron Back Scattered Diffraction (EBSD) allows to observe the grain orientation analysis and grain size measurement at specified locations of NZ before and after SHT. Back-scattered electron detector is used under 10keV working tension. EBSD cartography is performed on 100 µm by 80 µm areas, with pixel size of 0.1 µm and 0.75 µm for respectively high and low magnification observations. Non-indexed pixels are filled by extrapolation method based on the indexed neighbours. More than 10.000 NZ fine grains are measured at each position.

Micro-hardness testing allows characterizing the hardening η type precipitation. EMCO-test DuraScan G5 indentor implemented with the Vickers hardness standards under 0.3 kg loading (HV0.3) was selected for this study.

Tensile samples are obtained from the processed plates. Tensile testing is performed on a Zwick 250kN tensile machine. Loading displacement is imposed at 1mm/min. Tensile testing was performed for welds produced on the three different backing plates. Two types of samples are tested: in the transverse direction and in the welding direction. In the transverse direction, flat dog-bone sample have a squared reduced section 10 mm x 10 mm. The gage length is 30 mm taking the entire weld section. The tensile samples are machined by removing the exceeding 2mm of the initial aluminium plate. In the welding direction, cylindrical dog bone tensile samples are machined inside the NZ of the produced welds. Cylindrical samples are 6 mm in diameter for 30 mm gauge. All these samples were peak-aged using the referent T6 treatment, i.e.: 470°C for 30 minutes followed by artificial aging at 120°C for 24 hours. For the statistics, 3 tensile samples per condition are tested. In order to evaluate the ductility, post-mortem measurements of the fracture sample section were carried out to calculate the true fracture strain $\mathcal{E}_f = \ln(Area_0/Area_{fracture})$.

3. Results

3.1. Characterization of the base material

The 7475 alloy is composed of elongated textured grains. Impurities like iron-rich particles are distributed along the material. Figure 2 shows the three crystallographic orientations observed by optical microscopy: the longitudinal-transverse (LT), longitudinal-short (LS) and transverse-short (TS) planes. Grains are flatten following the rolling direction; the thickness of these pancake-like grains is roughly 50 µm, while their length and width is rising up to 1 mm for coarser grains.

Chemical content %wt											
	Al	Zn	Mg	Cu	Fe	Cr	Mn	Si	Ti	Ga	Zr
Al 7475	90.0	5.67	2.20	1.51	0.08	0.22	0.01	0.04	0.04	0.01	0.01

Table 3: Chemical analysis by ICP of 7475 base material expressed in weight percent

Table 3 provides the chemical composition measured by inductively coupled plasma optical emission spectroscopy (ICP). The 7475-T7 base-material presents a hardness of 171±4 HV0.3.

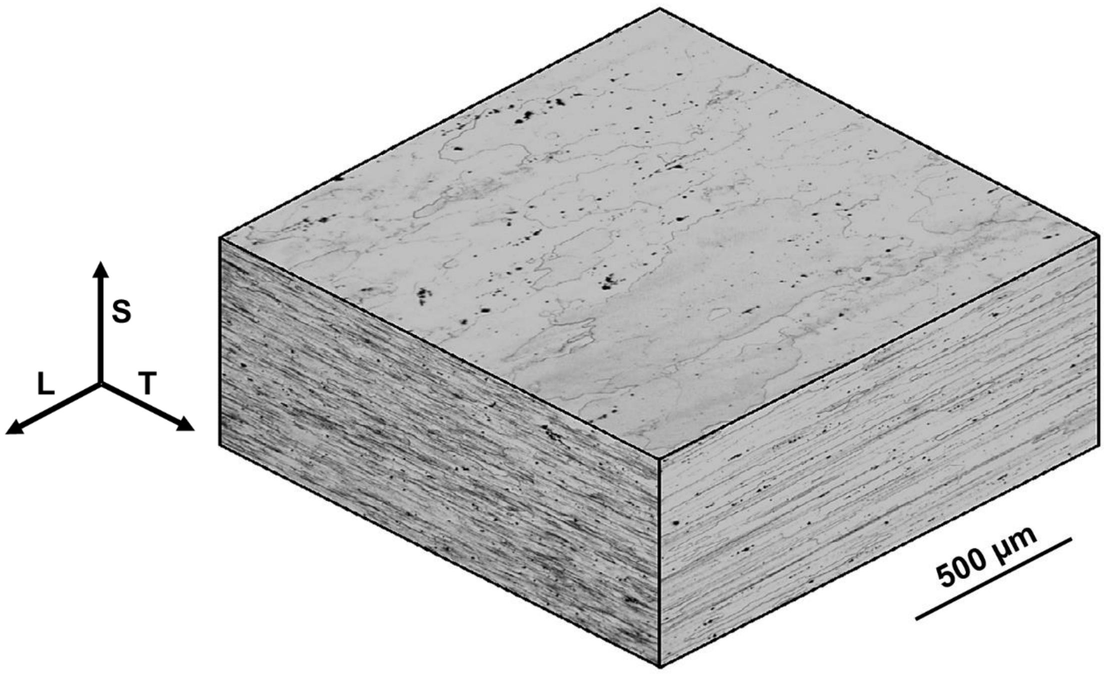

Figure 2: 7475 alloy microstructure: longitudinal-transverse (LT), longitudinal-short (LS) and transverse-short (TS) planes.

3.2. Temperature measurements during FSW

Figure 3 reveals the thermal cycle supported by the FSW weld for various backing plates. These measurements are taken at the bottom of the NZ (as schematized on Figure 1).

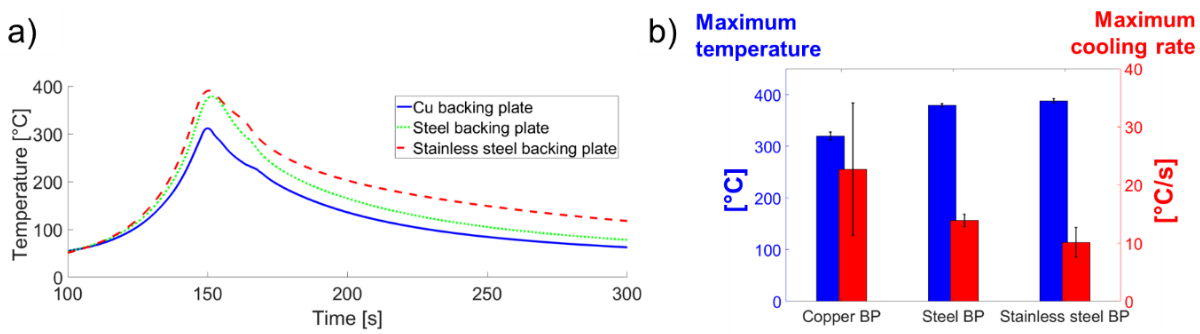

Figure 3: a) Temperature profiles depending on backing plate (BP) material, b) Maximum cooling rates during FSW, associated to peak temperature depending on BP, statistics on three measurements.

Figure 3 a shows the temperature evolution during FSW. The peak temperature is associated to the FSW tool crossing the thermocouple. It is higher for a stainless steel backing plate, then a steel BP and finally a copper backing plate. Such behaviour is in accordance with the thermal conductivity of the various backing plates (see Table 1). After the peak temperature, the three backing plate conditions have a similar exponential decrease of the temperature. Slow cooling is due to the significant amount of heat generated during the thick plate welding. Welds, backing plate and machine table need a few minutes to cool down to room temperature, oppositely to thinner welds. A copper backing plate weld is thus leading to cooler conditions; the stainless steel backing plate weld is reaching the highest temperatures throughout the entire cycle; the steel backing plate weld is leading to intermediate temperatures.

Figure 3 b is displaying the mean peak temperatures and maximal cooling rates at thermocouples position in function of backing plate. A copper backing plate weld is associated to 306 °C peak temperature, while a steel backing plate weld rises it up to 375 °C and a stainless steel backing plate weld up to 386 °C. Maximum cooling rates are obtained right after the peak temperature, when temperatures and thermal gradients are maximum. The cooling rate is decreasing for a Cu backing plate with a thermal conductivity of 360 W/mK compared to a stainless steel backing plate with a thermal conductivity of 15-20 W/mK. The maximal cooling rates measured are thus: 23 °C/s, 14 °C/s, 10 °C/s for copper, steel and stainless steel backing plates respectively. Knowing that the initial peak temperature is lower for a copper backing plate, the high cooling rate is really limiting the heat absorbed by the weld in comparison with the two other backing plates.

3.3. Microstructural characterization

3.3.1. Microstructure after FSW

Figure 1 presents the cross-section of bead on plate FSWed 7475 alloy. A 10 mm deep NZ is showing the typical onion rings microstructure. The TMAZ is also recognizable showing elongated grains. The HAZ is surrounding the weld. Figure 1 indicates the three zones of investigation in the NZ through the thickness of the weld. At these three locations, grains crowned by coarser η precipitates are clearly identifiable for the three different backing plates as displayed on Figure 4. Grains are much smaller in the bottom region for copper and steel backing welds; higher magnification is highlighting the sub-micrometre grains in these two conditions.

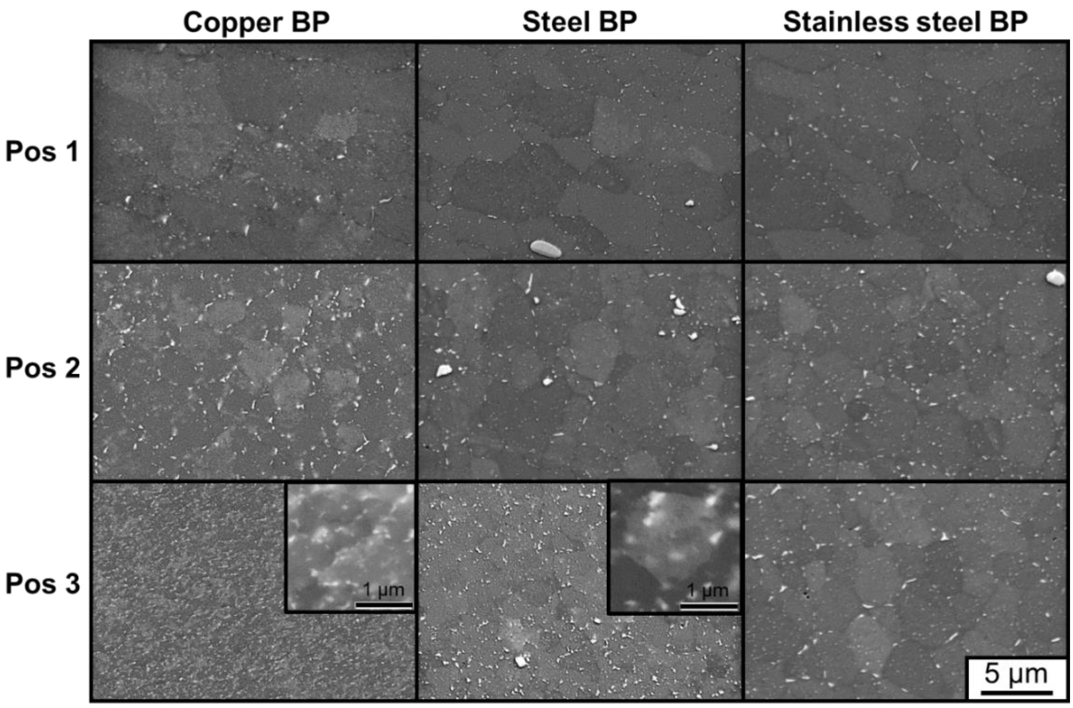

Figure 4: SEM images of as-FSWed microstructures at Pos 1 (top), Pos 2 (middle) and Pos 3 (bottom) for the three different backing plates (BP).

Figure 5 a shows the distribution of grain size in function of backing plate conditions and position (Figure 1). A mean grain size reduction from top to bottom of the nugget zones is observed for all the samples and displayed with standard deviation on Figure 5 b. The smaller grains are obtained via the copper backing plate welds at the bottom of the NZ, with grains presenting 0.5 µm of mean equivalent diameter. A stainless steel backing plate leads to more homogeneity in grain size. It is worth noticing that all samples have the same grain size in the top part of the weld, close to 2.8 µm equivalent diameter.

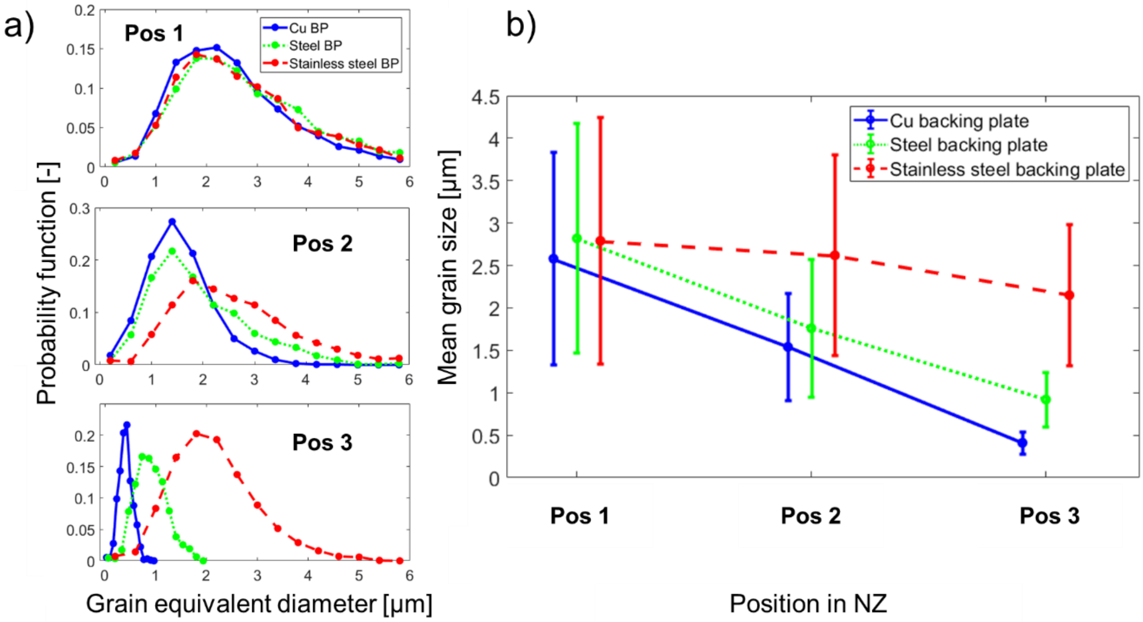

Figure 5: a) Grain size normal distributions according to position in NZ (Pos 1: top, Pos 2: middle, Pos 3: bottom, see Figure 1) and backing plate used (BP). b) Grains equivalent diameter quantified on SEM images, depending on backing plate (Copper, steel, stainless steel) and location in the weld.

Figure 6 a provides the mean size of coarse precipitates surrounding the grains. Sizes are classified in function of the three different backing plates and their locations. These precipitates are observed on further magnified SEM images, see Figure 4. The precipitates size is similar for all backing plates.

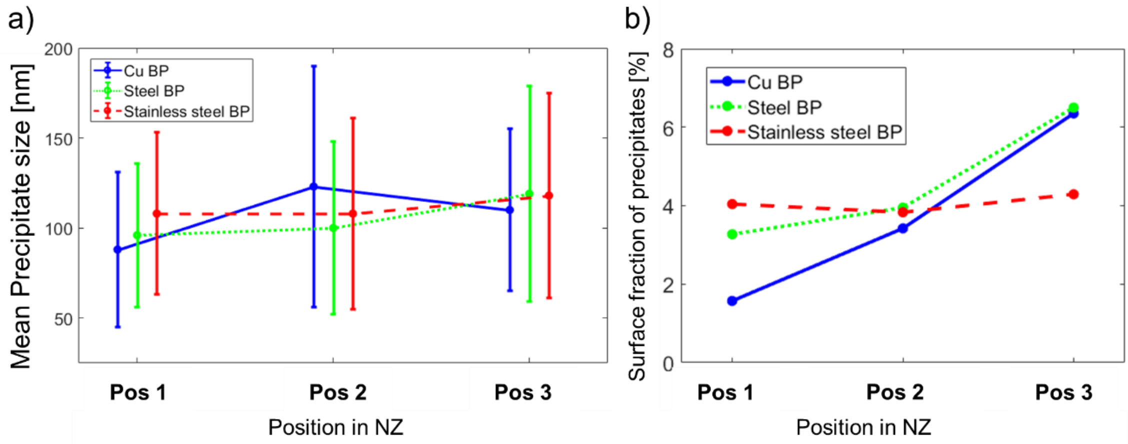

Figure 6: a) Coarse precipitates mean size; quantified by SEM images. Backing plate (Copper, steel, stainless steel) and location in the weld (Pos 1: top, Pos 2: middle, Pos 3: bottom, see Figure 1) are displayed. b) Surface fraction of hardening phase quantified on SEM images. Backing plate (Copper, steel, stainless-steel) and location in the weld are displayed.

Figure 6 b presents the surface fraction covered by coarse precipitates in the three samples at the three selected locations. For both steel and copper backing plate samples, the surface fraction is increasing from top to bottom of the NZ. The highest fractions of coarse precipitates corresponds to the smallest grain sizes, i.e. near the bottom part of the weld. The stainless steel sample has a more homogeneous surface fraction of precipitates through the thickness, similarly to the more homogeneous grain size.

The evolution of the coarse precipitation near the TMAZ transition at the bottom of the weld is highlighted on Figure 7**.** In the NZ-TMAZ transition zone, recrystallized grains and some fragments of the initially elongated grains are coexisting. No coarse precipitates are detectable inside the non-recrystallized grains while coarse precipitates have grown at grain boundaries in recrystallized regions.

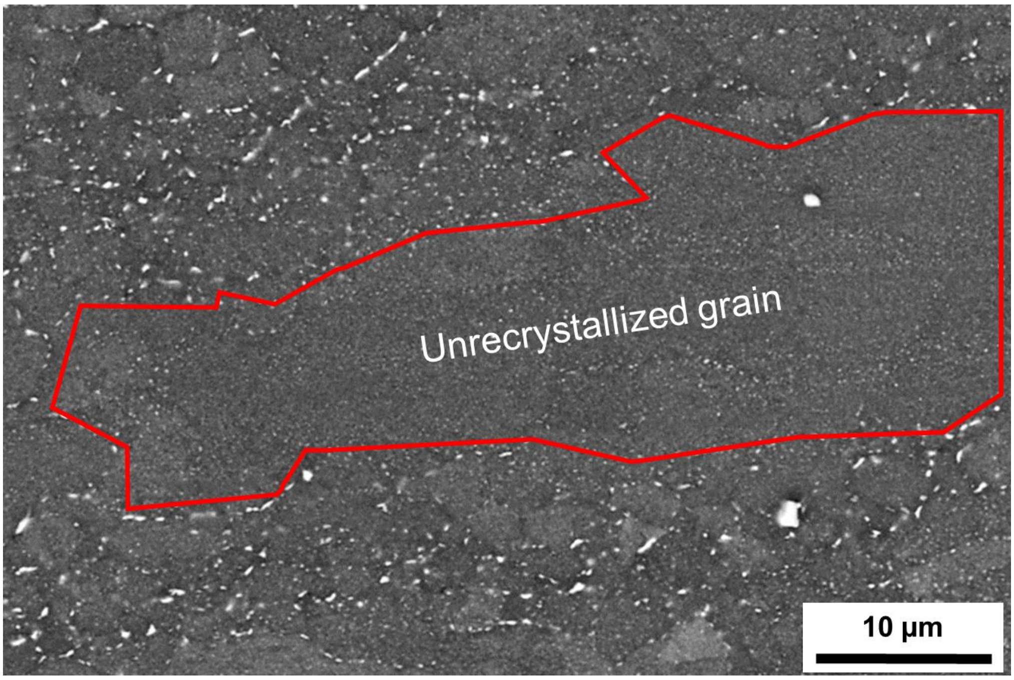

Figure 7: SEM image of transition region between NZ and TMAZ in Bottom region; elongated unrecrystallized grains and small recrystallized grains crowned by large precipitates co-exist. As-FSWed material, produced on stainless steel backing plate.

On Figure 8 a and b, EBSD measurements give the Inverse Pole Figure (IPF) maps for top and bottom regions of as FSWed Cu backing plate sample. The grain boundaries are associated to the IPF figures. Figure 8 confirms that dynamic recrystallization is associated to fine equiaxed grains with high angle grain boundary misorientation. The FSWed grains are thus independent of the initial textured grains. However, Figure 8 b is clearly dominated by the (101) orientation, meaning that a preferential texture exists in some locations of the NZ.

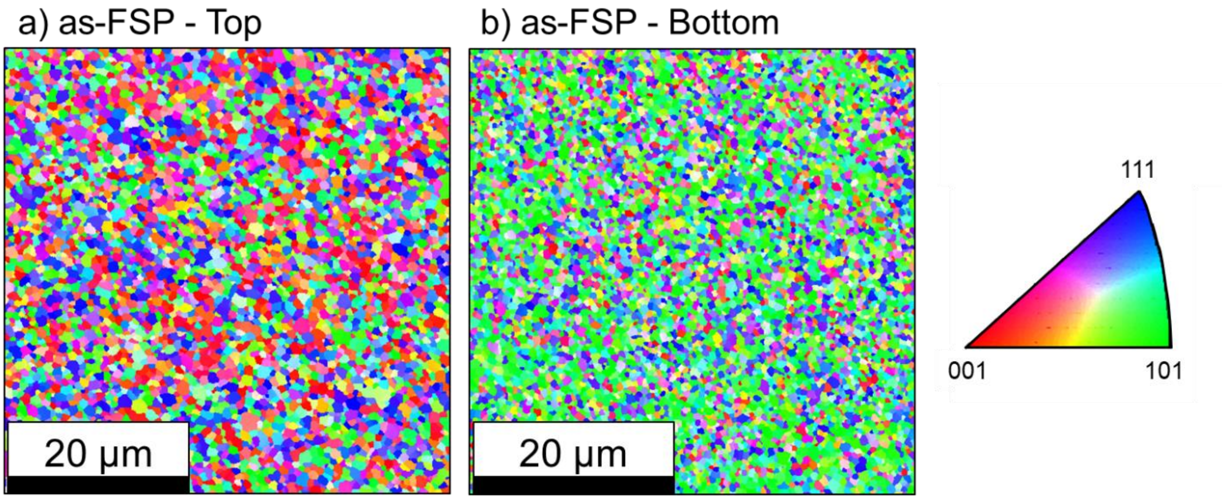

Figure 8: a) EBSD IPF map of top part of Copper backing plate NZ, b) IPF map of bottom part of Copper backing plate NZ, Copper backing plate sample.

As a concluding remark, the as-FS welded microstructures are quite similar in the top weld regions for the three backing plate welds. Then, the cooler conditions for copper and steel backing plate is leading to a refinement of the grains toward the bottom of the weld. A low cooling rate FSW condition (i.e. stainless steel backing plate) is associated to homogeneous microstructure in the entire thickness of the weld.

3.3.2. Effect of post-weld SHT conditions on secondary recrystallization

Figure 9 shows the secondary recrystallization of steel backing plate-processed samples, depending on SHT temperature (450, 470°C and 500°C). Such a backing plate is the usual choice and thus deserves additional attention. In the reference sample after a solution heat treatment of 30 minutes at 470°C approximatively 30% of the NZ is covered by coarse recrystallized grains. The higher the temperature, the higher the recrystallized part in the NZ for the same heat treatment duration. Recrystallization is not observable after 5 min for all tested temperatures. Then, the recrystallized area is expending with the heat treatment duration. Recrystallized grains have a tendency to grow following onion rings. It is particularly true near the advancing side (on the left part of welds in Figure 9).

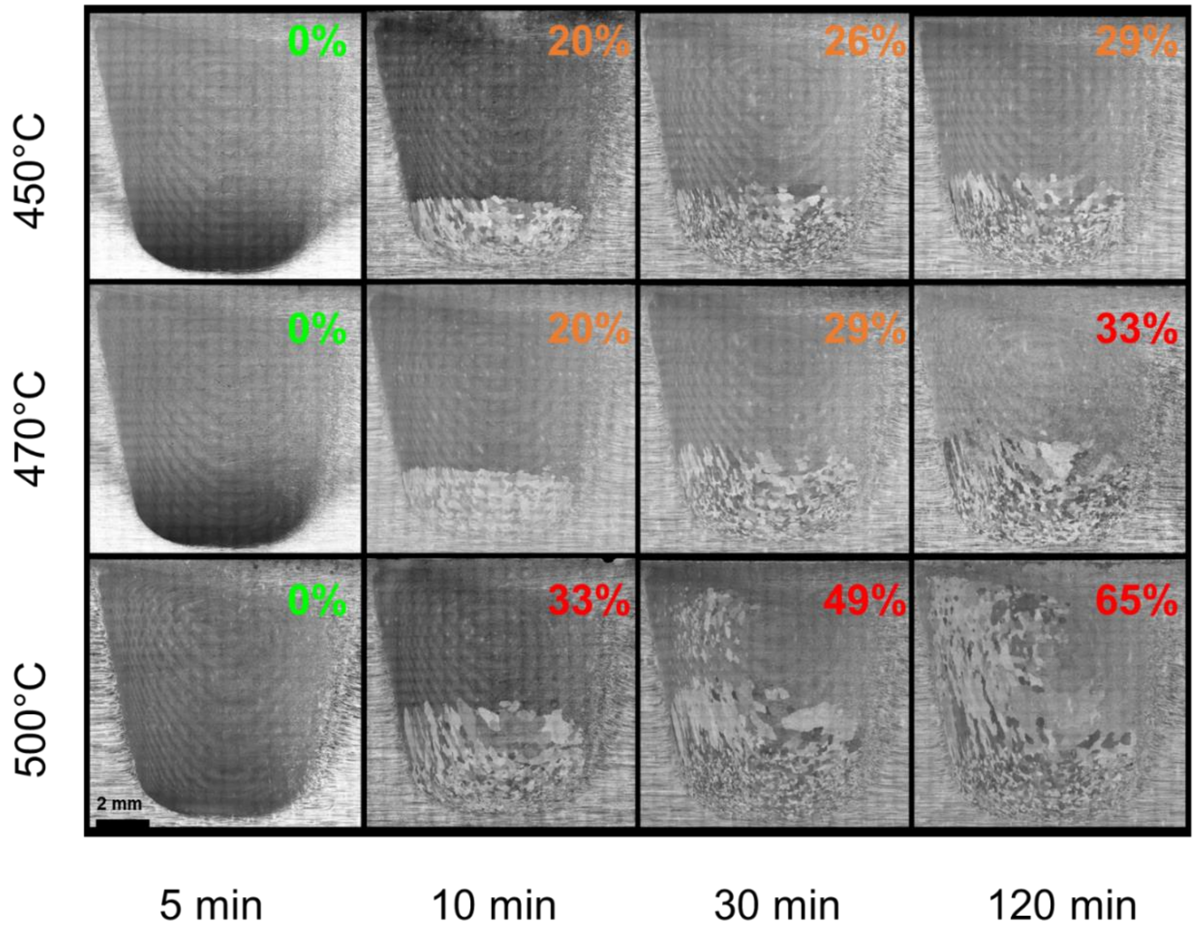

Figure 9: Steel BP sample showing secondary recrystallization as function of time and temperature, NZ recrystallized area in %. Steel backing plate welding condition. Advancing side is on the left.

Recrystallized area is reaching a maximum 65% of the initial NZ in the case of 500°C SHT for 2h. It is twice the value obtained for 450°C and 470°C SHTs for the same duration.

Figure 10 shows the evolution of the amount of secondary recrystallization during a very slow heating rate (3.3 °C/hour) applied to a steel backing plate weld. Samples were extracted at various temperatures. The coarse secondary recrystallization temperature lies between 370°C and 380°C for this weld microstructure. In a 10°C range, recrystallization is already consuming a significant part of the fine grains, 12% of the NZ surface. This proportion is increasing with temperature up to 32% recrystallized NZ surface. This result proves that a low heating rate is not a solution to avoid or reduce secondary recrystallization in comparison with the standard

SHT. Thus, the heating rate sensitivity observations reported by Hassan *et al.* and introduced in introduction section (see section 1.5) is not observed [21].

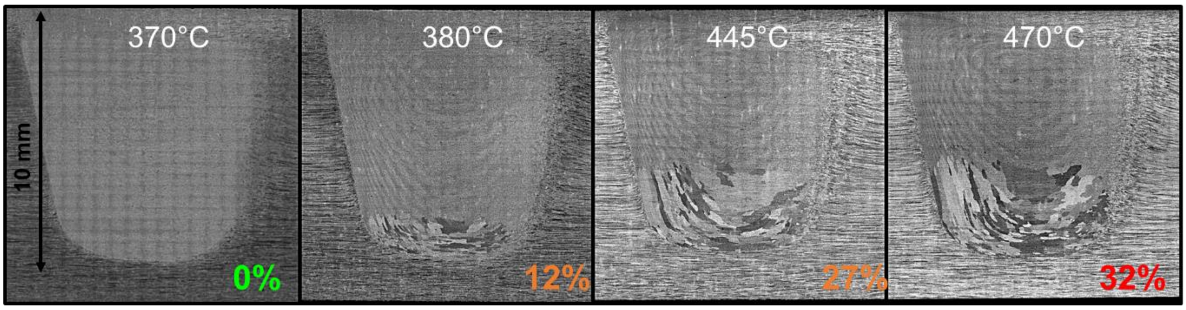

Figure 10: Steel BP sample evolution of secondary recrystallization with continuous heating. Heating rate = 3.3°C/h. Recrystallized area fraction of NZ in % at given temperature. Steel backing plate welding condition. Advancing side is on the left.

Figure 11 a and b show post-SHT material, after 30 minutes at 470°C. The IPF results are displayed for the transition zone between coarse and fine grains as well as for the coarse grains area. Cu backing plate was used to manufacture the samples. After SHT, the remaining fine grains of Figure 11 a had still a micrometric diameter. The coarse recrystallized grains are identified on Figure 11 b.

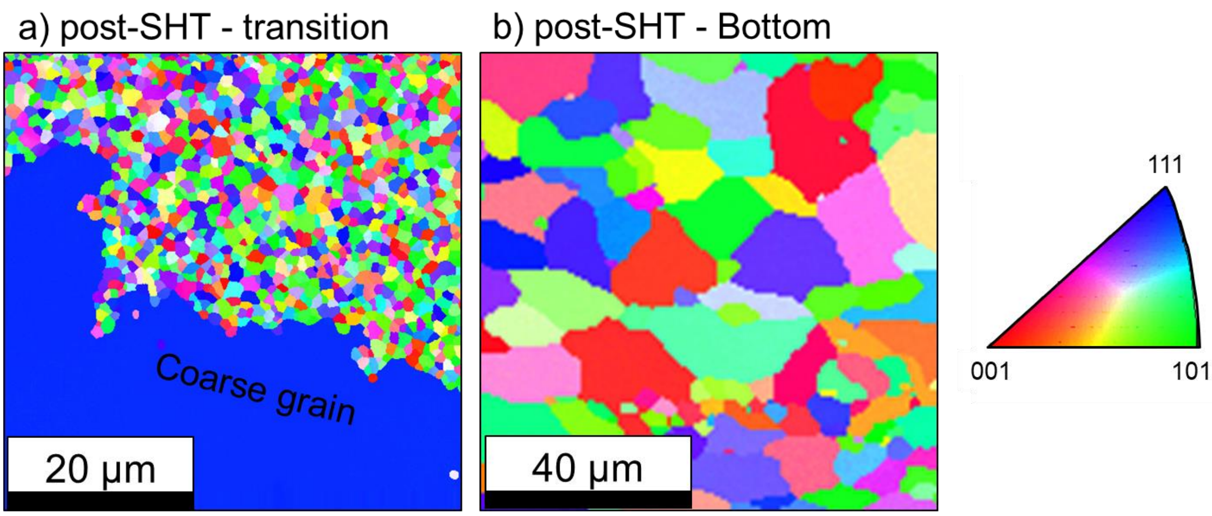

Figure 11: a) EBSD IPF map of transition zone between AGG – fine grains after 30 minutes SHT on Copper backing plate sample, b) IPF map of recrystallized grains after 30 minutes SHT on Copper backing plate sample.

Figure 12 shows the influence of the backing plate selected on secondary recrystallization during post-weld heat treatments. SHT is performed in the reference conditions, i.e. 470°C for

30 min. Copper, steel and stainless steel backing plates are generating respectively 40%, 20% and 0% secondary recrystallization fraction. It is thus possible to generate, even with a high temperature solution heat treatment of 470°C, a weld exempt of secondary recrystallization.

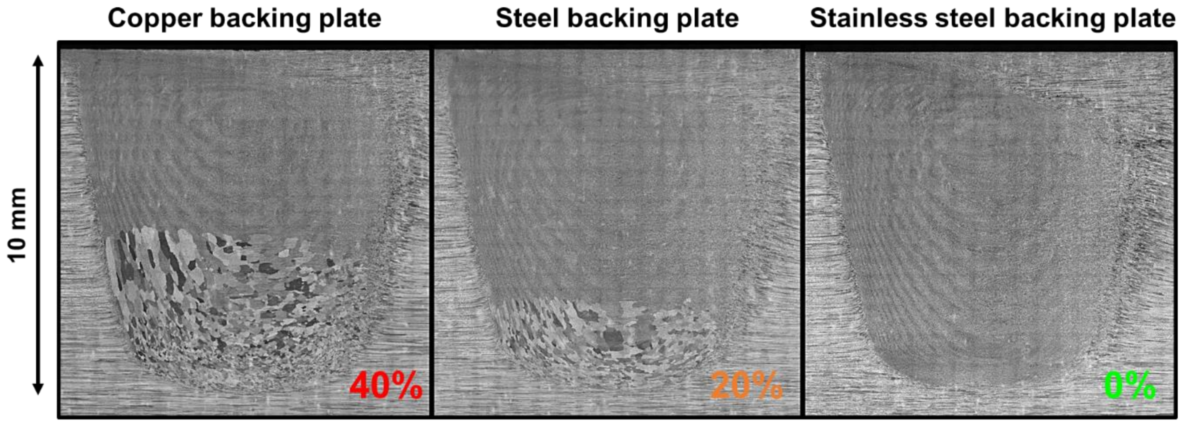

Figure 12: Effect of backing plate on secondary recrystallization during post-weld solution heat treatment performed at 470 °C for 30 minutes: copper, steel and stainless steel backing plate welds. Recrystallized area fraction of NZ in %. Advancing side is on the left.

According to Figure 5 b, the stainless steel backing plate weld is leading to coarser grains in the bottom part of the weld, around 2.5 µm. Five times coarser than the grains of the Cu backing plate weld, these larger grains (2.5 µm) are thus recrystallization and AGG resistant during SHT.

Now, one may point out that 5 minutes at temperature from 450°C to 500°C do not lead to secondary recrystallization for a classical steel (Figure 9). However, the SEM image of Figure 13 a shows that the 5 minutes SHT at 470°C is not dissolving the hardening precipitation which is the aim of a SHT. Figure 13 b shows that most precipitates have dissolved after 10 minutes at 470°C, and the grains have grown on 20% of the NZ surface, as displayed on Figure 9 (10 min – 470°C). Figure 13 c is highlighting that a SHT at 370°C is affecting drastically the precipitation, leading to Al-Cu-Mg rich phase (probably S phase) according to EDX measurements of Figure S2 (supplementary material). Notice that Zn concentration is low in the precipitates, even lower than into the matrix, meaning that Zn is already dissolved in the matrix at 370°C. Figure 13 d is finally showing that a SHT at 380°C is leading to AGG even though the coarse precipitation is still visible. None of these treatments are acceptable to reach the strongest T6 state in the NZ.

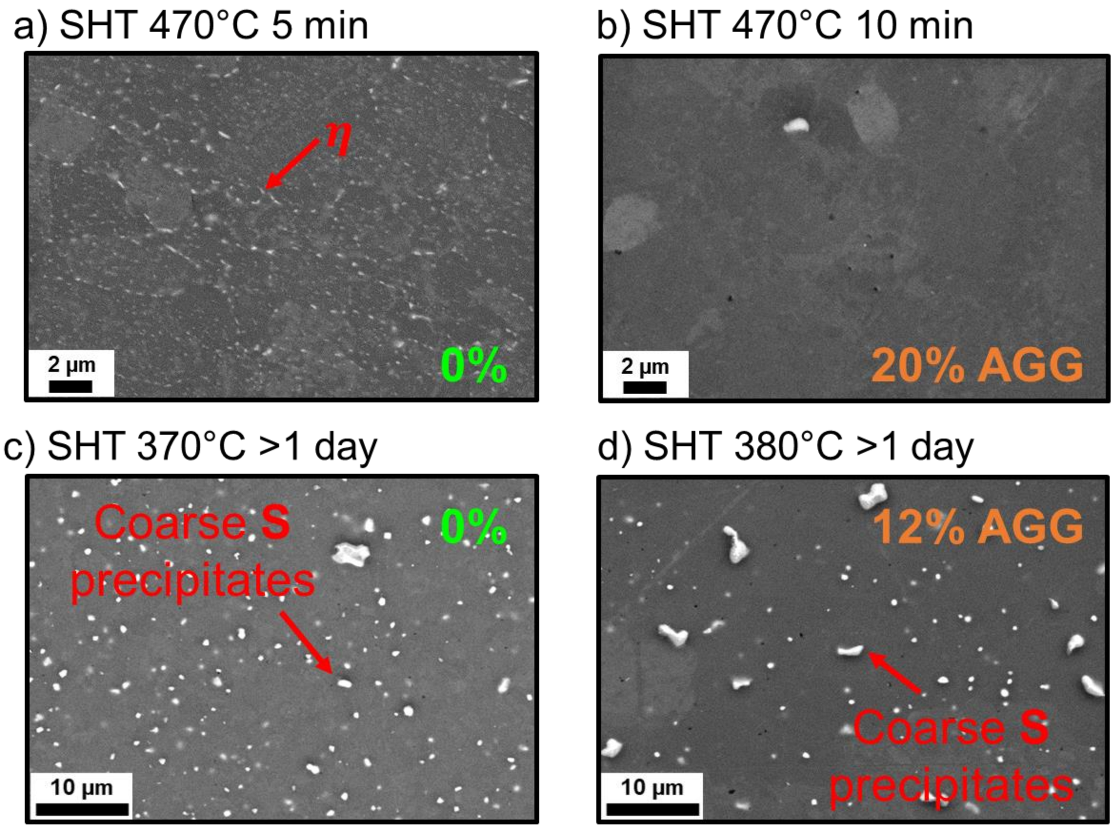

Figure 13: Effect of SHT conditions on precipitates: a): 5 minutes SHT is not sufficient to dissolve as-FSWed precipitation. b) 10 minutes at 470°C dissolves the coarse precipitation but AGG is detected. c) 370°C and d) 380°C long duration treatments are forming coarse S phase particles; d) AGG is detected. Steel backing plate welding conditions.

As a conclusion of the SHT results: short duration heat treatment of 5 minutes is preventing AGG or recrystallization. However, the SEM images of Figure 13 reveal that the hardening precipitates are not dissolved. Same observation for 370°C SHT on Figure 10: coarser precipitates are generated at that temperature. The only path to dissolve precipitates and still preserve the small grains is the use of a stainless steel backing plate condition (Figure 12). Low cooling rate FSW condition, obtained by the stainless steel backing plate, prevent grain growth during SHT. This will be further discussed in section 4.2 and in particular in subsection 4.2.4. In what follows, standard SHT of 470°C for 30 minutes will be used. Further artificial aging of 24 hours at 120°C rises the mechanical properties of the welds to the T6 state. The T6 state reveals the full mechanical performances of this alloy while the various backing plates conditions will highlight the effect of recrystallized grains ratio on mechanical properties.

3.4. Mechanical properties

3.4.1. Hardness measurements

Figure 14 shows the hardness profile of the weld after FSW, in function of the three different backing plates, for the transverse or thickness direction and before and after the T6 heat treatment. All samples are affected by the heat generated during FSW. On Figure 14 a, horizontal mid-thickness HV0.3 profile is highlighting the low hardness of the HAZ, while the TMAZ and NZ have higher hardness in the as-FSWed state. In comparison, the base material is known to reach 171 ± 4 HV0.3 in the T7 state. The entire weld area is thus softened but a copper backing plate welding condition leads to higher hardness in the NZ and HAZ. On Figure 14 b the NZ is reaching a maximum of 150 HV0.3 hardness near the top part with a copper backing plate, while a stainless steel backing plate weld reaches only 135 HV0.3 at the same location. A steel backing plate gives an intermediate 140 HV0.3 NZ. In both directions, the copper backing plate is maximizing the hardness obtained after FSW.

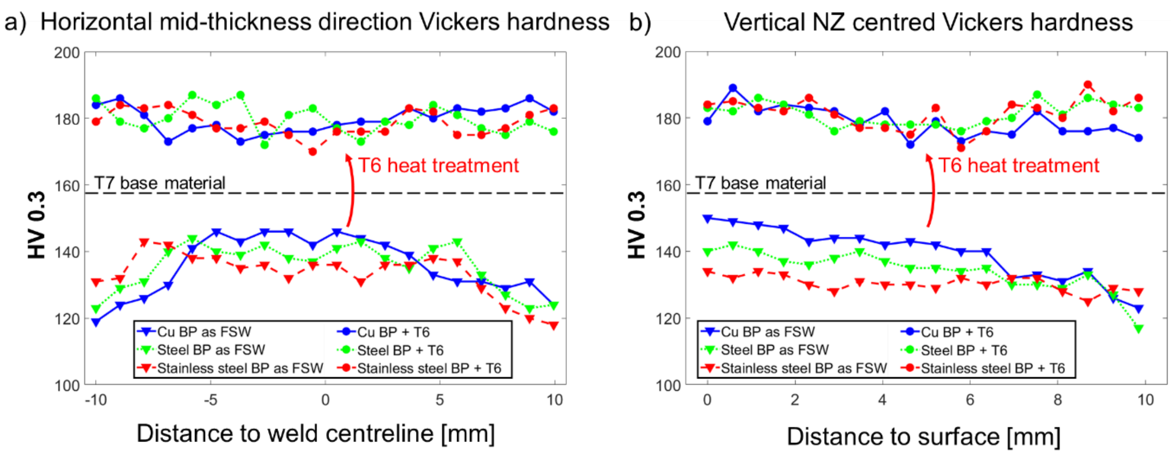

Figure 14: a) Hardness measurements along mid thickness transverse direction. b) Hardness measurement through the thickness from top to bottom. As FSWed samples present hardness variation while T6 heat treated samples are homogeneous and harder. T7 hardness of initial 7475 material is displayed with dash line.

Figure 14 b confirms that the NZ hardness is more homogeneous in the depth direction in the case of a stainless steel backing plate but this configuration is softer than the other as-welded conditions. For copper and steel backing plate samples, hardness is decreasing from top to bottom of the NZ. This decrease is more evidenced in the copper backing plate condition, dropping down to 125 HV0.3 at NZ bottom area. It is worth mentioning that steel and stainless steel backing plate welds have the same hardness as copper backing plate welds at the bottom of the NZ.

Figure 14 a and b are showing hardness evolution after T6 heat treatment. The SHT 470°C for 30 minutes and artificial aging at 120°C for 24 hours is rising the hardness in the transverse and thickness directions. Both directions are reaching the same hardness without significant variation through the weld section. A T6 state hardness is reached uniformly despite microstructural variations along the weld. The hardness is reaching up to 180 HV0.3 for each backing plate. This corresponds to the hardness of the base material in T6 state. By applying the T6 treatment, the material is reaching more homogeneous properties through the entire weld, leading to higher mechanical strength.

3.4.2. Tensile test results

Figure 15 a presents the tensile curves obtained for a weld transverse loading for the three types of backing plates. All samples were solutionized at 470°C for 30 minutes and peak-aged (120°C for 24 hours), leading to the usual T6 yield stress of 500 MPa [3]. The three samples are following the same behaviour in transverse tensile loading. All conditions are reaching the same ultimate tensile stress before localization: $\sigma_u = 550$ MPa.

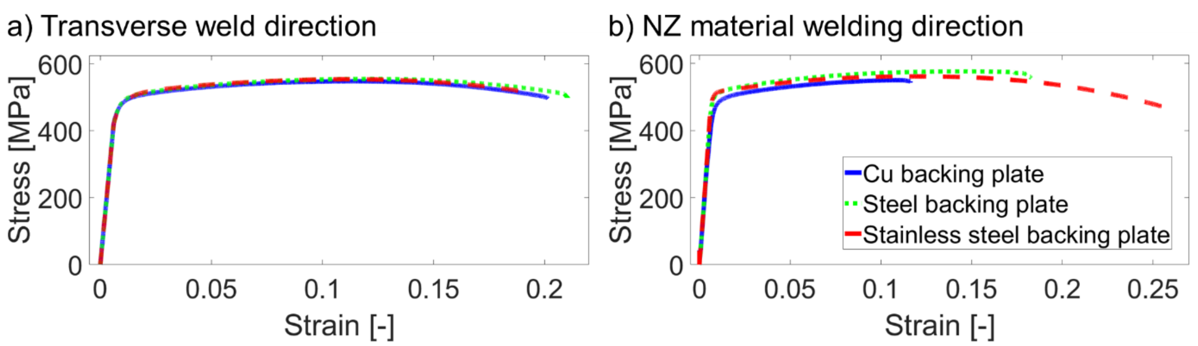

Figure 15: Tensile curves a) in transverse direction in function of the backing plates used; b) in NZ welding direction in function of backing plates. SHT treatment and artificial aging performed prior to tensile test, at 470°C for 30 minutes + 120°C for 24 hours.

Localization of strain is generating a neck for all samples. This localization happens in the HAZ – TMAZ regions. Elongation is similar for all samples, around 38 ± 2 % expressed in true fracture strain. This is expected to be due to differences in the strain hardening behaviour of the HAZ-TMAZ compared to the NZ. In a 6005A alloy, Simar *et al.* [35] have shown that a similar hardness in the HAZ, the TMAZ and the NZ but a different strain hardening ability could indeed lead to strain localisation in the TMAZ.

Concerning fracture path, fracture occurs through the HAZ. Some of the steel backing plate and copper backing plate welded tensile samples have their crack path influenced by the abnormal grains in bottom of the NZ. Figure 16 displays the cracked copper backing plate sample, polished in transverse – thickness direction. One can see that the fracture path is clearly influenced by the coarse grains inside the NZ.

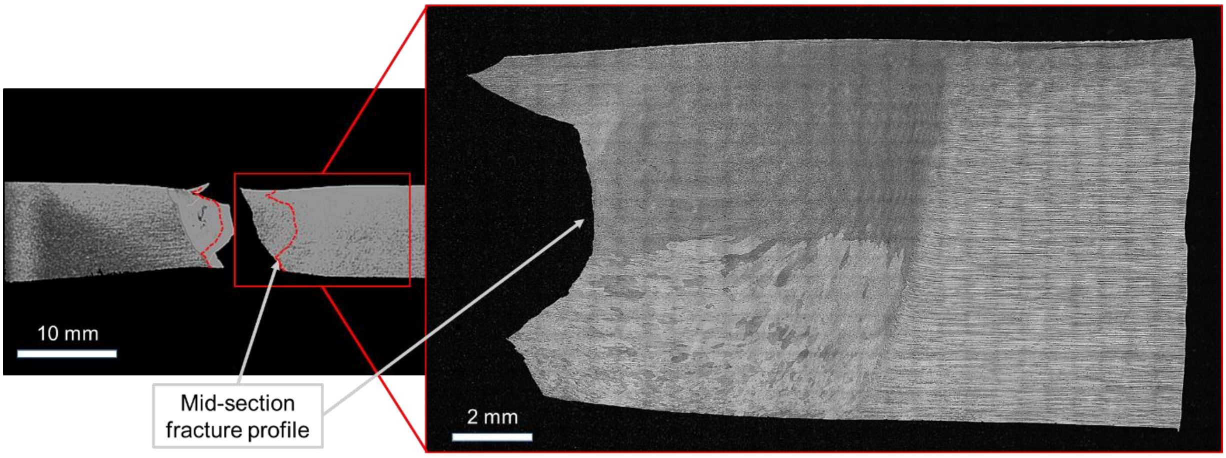

Figure 16: Copper backing plate influence of microstructure on the crack propagation, optical microscopy. Left: overview of the broken sample and mid-section fracture profile highlighted. Right: polished mid-section broken sample showing microstructure impact on crack path.

Figure 15 b displays the tensile curves of the NZ-only material for all backing plate conditions after the same SHT and peak aging. The longitudinal properties are highly affected contrarily to the transverse tensile properties in the NZ. The copper backing plate sample is leading to early fracture of the tensile sample with a true fracture strain of 24.0 ± 3.5 %. Welding on a steel backing plate also limits the fracture strain: 25.5 ± 5.3 %, while a maximum fracture strain of 46.7 ± 10.0 % is reached for the stainless steel backing plate welded tensile samples.

Fractographic SEM images of longitudinal direction tensile samples are shown on Figure 17. The surface of broken samples are highlighting the influence of the recrystallization in the damage mechanisms. Flat areas are observed on copper and steel backing plate welded tensile samples. These flat regions are related to the coarse grain failure. In such samples, ductility is reduced in comparison with the stainless steel backing plate NZ tensile samples.

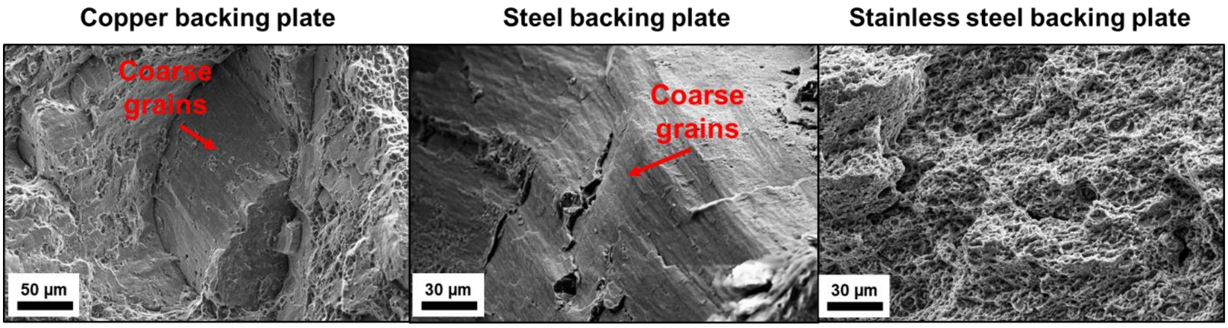

Figure 17: Fractography of tensile samples in function of the backing plate. Coarse grains have left a flat surface when the material failed for copper and steel BP NZ tensile samples. A stainless steel BP gives a fine and homogeneous ductile crack path, showing fine dimples.

4 Discussion

This section is focussing on essential aspects that play a role in the excellent behaviour of stainless steel backing plate welds. Secondary recrystallization mechanisms (either normal or abnormal grain growth) are leading to strong variations in microstructures, as observed in Figure 9, Figure 10 and Figure 12. These mechanisms are affected by the FSW initial heat cycle. Recrystallization is influenced by the selected SHT parameters applied in this work. Controlling and limiting grain growth during SHT results in excellent weld performances, with 100% yield strength compared to a 7475 alloy inT6 state.

4.1. Linking thermomechanical conditions with microstructural features for the various backing plate conditions

4.1.1. Processing conditions leading to heterogeneous microstructures

The thermomechanical cycles due to FSW are affecting drastically the microstructure of the 7475 alloy. Due to heat and plastic deformation, the initial elongated grains are dynamically recrystallizing into finer equiaxed grains. Figure 1 and Figure 4 have shown that the entire NZ is subjected to the dynamic recrystallization phenomenon whatever the backing plate selected.

As the backing plate and parent material are absorbing the produced heat, a thermal gradient is associated to FSW. In the three investigated backing plate configurations, the bottom part of the NZ should reach lower temperatures compared to the top part, according to Mishra *et al.* [4]. The present experimental conditions are influencing temperature in the NZ. Figure 3 b highlights the maximum cooling rates in function of backing plate. Consequently, as more heat is absorbed by the backing plate, the maximum temperature recorded at thermocouple position reduces as showed on Figure 3 a. This is in good agreement with Martinez *et al.* [14], who identified larger temperature gradients with thicker welds due to the high thermal conductivity of aluminium.

4.1.2. Grain size

According to Figure 5 b and EBSD maps in Figure 8, the copper backing plate weld presents the smallest grains of this work, around 0.5 µm diameter, which is in accordance with Rhodes *et al.* who have quantified grain size in function of heat cycle in 7050 alloy [27]. Rhodes obtained roughly 0.4 µm grains after 1 minute at 350°C, similar to the bottom of the copper backing plate weld. For each backing plate sample of Figure 4, FSW generates coarser grains at the top of the NZ. Grain size measurements in Figure 5 b show that in top regions the grain size is around 2.8 µm, independently of the backing plate material. As the tool shoulder generates most of the heat according to Mishra *et al.*, all samples have reasonably similar maximum temperatures in their top part [4]. Lower temperature and higher cooling rate of Figure 3 are coherent with a grain size decrease from stainless steel to copper BP welds, accentuating the thermal influence of temperature on grain size.

4.1.3. Coarse precipitation

Figure 4 confirms that coarse precipitates are present on the grain boundaries of NZ dynamically recrystallized grains in accordance with Su *et al.* and Martinez *et al.* [10][14].

Inversely, Figure 7 shows that restored grains are not containing coarse precipitates in the grain interior, as explained in introduction section 1.3. It was previously reported that these coarse particles are η non-coherent phases [10][14].

Figure 6 a reveals that the precipitates size is rather homogeneous in the thickness direction, typically around 100 nm. Kamp *et al*. have modelled the precipitation state after FSW in 7449 alloy [36]. They concluded that precipitates are reaching a stable size and stable volume fraction in approximately 50 seconds after maximal temperature. In this delay, precipitates grow up to 90 nm diameter. This is in good agreement with the results of Figure 6 a. However, Martinez *et al*. noticed that the thickness of a 7449 weld impacts the fine precipitation microstructure [14]. They measured finer precipitates in the bottom of the NZ [14]. Furthermore, slow cooling is generating coarser precipitates according to Kamp *et al.* [36]. Hotter regions of the weld should present coarser precipitates because of slower cooling. This was also demonstrated on 2XXX alloys by Avettand-Fenoel *et al.* [26]. Nevertheless, this is in contradiction with the present work observations reported in Figure 6.

As a first attempt to understand homogeneous mean size of precipitates despite temperature variations, an interesting result is drawn on Figure 6 b. The graph is demonstrating an increase in surface fraction of coarse precipitates in the bottom part of the NZ for copper and steel backing plate samples. A higher density is counter-intuitive with the fact that temperatures are supposed to be lower in these regions (according to Mishra *et al.* and Martinez *et al.* [4][14]). The reason is probably related to (high angle misorientation) grain boundary preferential precipitation, as the bottom region presents smaller grains for the Cu and steel BP samples, i.e. a higher density of grain boundaries.

In 7475 alloy, η precipitation is highly sensitive to grain boundaries. As 7XXX series segregate alloying elements at grain boundaries [2], the density of grain boundaries affects precipitates population. In order to measure the influence of the grain boundary, Figure 7 is a key. Both small recrystallized and restored coarse grains are coexisting, showing higher η precipitates density in small grain region. Both fine and coarse grains are existing at the same location, thermal history is supposed to be identical in both microstructures. It is thus established on Figure 7 that the higher the high angle misorientation grain boundary density, the higher the density of coarse precipitates.

The distribution of η precipitates is also linked to the hardness profile. Figure 14 b is showing softening of the weld NZ in the bottom region for copper and steel backing plate welds, corresponding exactly to higher precipitates density region. Effectively, alloying element are trapped extensively at grain boundaries at the bottom part of the weld. Dense grain boundary regions suffer from a huge depletion of solute elements and thus the material softens. The stainless steel backing plate prevents this softening in depth direction because the entire weld is subjected to more homogeneous grain boundary and η precipitation density, according to Figure 5 b and Figure 6 b.

As a summary of the as FSWed microstructures, the following trend lines can be drawn: grain size of Figure 5 b is related to precipitation density of Figure 6 b. Small grains are associated to higher precipitation density. Post FSW cooling is affecting grain size but not precipitation size. Grains are forming first; precipitates are then nucleating and coarsening at the newly formed grain boundaries in the first dozens of seconds after peak temperature. This results in a highly heat affected precipitation state leading to the observed softening in the weld nugget, TMAZs and HAZs. This is the motivation to use SHT on welds, allowing to fully dissolve the coarse η precipitates. After a subsequent low temperature aging treatment, a homogeneous T6 precipitation state throughout the entire weld section may be achieved.

4.2. Secondary recrystallization during SHT

4.2.1. Effect of the dissolution of pinning particle

In order to explain the sudden coarsening observed on Figure 9 between 5 and 10 minutes SHT, literature focussed on pinning particles dissolution threshold leading to grain coarsening, as presented in section 1.6 [19][20][21][28].

An initiation threshold is identified on Figure 10, where secondary recrystallization is evidenced between 370 and 380°C. However, dissolution of pinning (hardening) precipitates in 7050 and 7075 alloys starts at 300°C according to Fuller *et al*. [37]. This dissolution temperature is obviously at a lower temperature than the identified recrystallization threshold on Figure 10. Looking at the hardening precipitation, SEM observations on Figure 13 c and d prove that coarsen precipitates are present and are equivalent before and after the AGG initiation of Figure 10. Precipitation state being similar, the pinning effect of these very coarse precipitates (diameter of the order of 1 µm) is thus not expected to be the main mechanisms preventing grain growth.

However, at higher temperature but high heating rate SHT, Figure 13 a and b show that 5 minutes duration SHT is not sufficient to dissolve the coarse post-FSW precipitates (~ 100 nm), while 10 minutes is sufficient. In that situation, dissolution of the precipitation corresponds to secondary recrystallization initiation. Probably that post-FSWed fine precipitates pinning effect is decreasing until full dissolution, allowing initiation of (abnormal) grain growth.

4.2.2. Temperature effect

Looking at Figure 9, a significant amount of recrystallized grains are observed after 10 minutes SHT for all temperatures. Extended SHT duration to 120 minutes is not affecting significantly the recrystallized proportion at 450°C and 470°C, suggesting that this recrystallization is a sudden phenomenon once SHT temperature is reached, taking place in a few minutes as also proposed by Sun *et al.* and detailed in section 1.5 [25]. Furthermore, Figure 10 shows the final recrystallized area is covering 32% of the NZ after very low heating rate and thus very long SHT duration, which is close to the 29% ratio obtained with the short duration treatments of 30 minutes in Figure 9.

The main parameter influencing AGG proportion in this work is subsequently the SHT temperature. Recrystallized fraction obtained at 450°C roughly become twice this amount for the same SHT duration at 500°C, as highlighted in Figure 9. The higher the temperature, the higher the recrystallized area. This is in accordance with Huang *et al.* who proved that secondary recrystallization is sensitive to SHT temperature, because temperature affects the grain boundary mobility during secondary recrystallization [13].

4.2.3. Heating rate effect

Comparing Figure 9 and Figure 10 allows to identify that a fast heating rate for SHT at 470°C leads to slightly smaller recrystallized coarse grains. Indeed, Figure 10 is showing coarser grains than for the 470°C sample in Figure 9. This is in accordance with Hassan *et al.* who comparatively have proven that a very high heating rate (500°C/s) is leading to smaller coarse grains compare to lower heating rates (100°C/s), see section 1.5 [21]. They state that lower heating rate can activate more distinctly the coarsening of a few grains by the dissolution of part of the pinning precipitates. As higher heating rate favours the nucleation of more numerous coarse grains, the growth potential is thus limited by the higher density of coarsening grains.

4.2.4. Grain size impact on AGG-recrystallization

Homogenization of grain size due to the stainless steel backing plate is displayed on Figure 5. The stainless steel backing plate is leading to efficient welds without detected coarse grains after SHT on 7475 alloy as shown on Figure 12. Hu *et al.* [19] also prevented AGG on a more homogeneous NZ microstructure on 2024 alloy [19], see section 1.7.

In this work, Figure 5 b combined with Figure 12 have proven that 2.5 µm grains obtained via stainless steel backing plate are stable during solution heat treatment. Further EBSD measurements of Figure 8 evidenced on copper backing plate sample that surviving small grains after SHT had a 1.0 ± 0.4 µm diameter. The stable grains in 7475 samples are at least 10 times finer than grains characterized by Hassan *et al*., while stable grains of Stainless backing plate sample are 2.2 ± 0.8 µm, still much smaller than literature results [21]. Indeed, Hassan reported that grain size should be larger than 10 µm to be resistant to secondary recrystallization during SHT [21].

As finer grains are more prone to recrystallization, according to Figure 5 combined with Figure 12, the thermal analysis reveals that these regions were subjected to cooler temperature and higher cooling rates during processing according to Figure 3. This is in accordance with Mishra *et al.* [4]. Consequently, grains have less time to grow compared to top regions of the NZ. The very fine grains are thus unstable, with energy stored in this very fine microstructure according to Liu *et al.* [17]. Coarsening is thus easier in these particular unstable regions compared to coarser and more stable grains, i.e. on top part of the NZ, what is evident on Figure 9. As a proof of the link between grain size and secondary recrystallization, Liu *et al*. is exploring water submerged FSW conditions, leading to extremely fine unstable grains that systematically turn to coarse secondary recrystallized material after SHT [17].

4.2.5. Other microstructural parameters

In this work, Figure 9 and Figure 10 are showing some preferential growth along the onion rings structure that are showing lower misorientation angle boundary in circumferential direction according to Huang *et al*. and described in section 1.6 [13]. EBSD investigations of this work did not highlight the texture variation at the investigated scale, as displayed on Figure 8. However, Figure 8 b indicates that a (101) texture dominates in the bottom zone of the sample, while the top part is rather showing random orientation of the grains, as observed by Xu *et al.* on thick 7085 welds [11].

4.2.6. Evaluations of proposed solutions to avoid AGG

In all anti-recrystallization strategies in the literature detailed in the introduction section 1.7, the main objective is to build a more homogeneous microstructure, by lowering thermal gradients and improving plastic fluxes when stirring [13][19][20][21][28]. In this work, this objective was simply achieved by changing the backing plate. Figure 5 and Figure 6 are demonstrating that stainless steel backing plate is generating a more homogeneous microstructure in terms of grains and precipitates. The homogeneous microstructure is then recrystallization resistant after SHT, as displayed on Figure 12.

4.2.7. Take home message

As a conclusion, small grains under a specific size are the microstructural feature associated to secondary recrystallization. The small size is generated by lower temperatures and higher cooling rates conditions after FSW, conditions that lead to heterogeneous microstructure, plastic deformation and grain stored energy.

4.3. Mechanical properties of welds: towards high strength 7XXX welds

The present work has successfully improved 7XXX welds performances by applying SHT on welded material without AGG. Compared to Sajadifar *et al.* full strength welds (see section 1.4), ductility in significantly increased by the control of the cooling rate via stainless steel backing plate [22].

According to Figure 15, tensile performances of T6 welds reveal that transverse and longitudinal directions are not equivalent. All weld conditions, independently of backing plate, are providing high performances in transverse direction. This result is contrasted with longitudinal tensile properties, in the NZ. In that case, the influence of the backing plate is highly pronounced. On Figure 17, it is obvious that copper and steel backing plate welds are generating detrimental coarse grains during SHT, leading to premature failure. Recrystallization leads to roughly 50% coarse grains in NZ and acts as a preferential crack path, as exposed on Figure 16. Oppositely, the stainless steel backing plate weld is reaching extremely high ductility in comparison to the two other cases. Avoiding recrystallization is leading to excellent NZ behaviour in welding direction.

This work reveals the importance to control the (abnormal) grain growth in post-FSW SHT. By playing on heat cycle via backing plate exchange, optimized FSW parameters can be used to produce AGG resistant grains. Previous studies were trying to catch good FSW parameters via extensive experimental campaigns, while only the backing plate temperature and heat conductivity parameters suffice to control the microstructure. Knowing the grain size threshold for recrystallization, backing plate thermal conditions can be tuned to produce homogeneous grains along the entire NZ.

5. Conclusion

FSW bead on plate welds were successfully manufactured; exchanging the backing plate material. The heat cycle during FSW is modified, particularly in the bottom part of the weld, near the backing plate. The following points highlight the results:

- Copper backing plate weld results in the finest grain structure.

- Stainless steel backing plate weld allows a higher temperature in the bottom region of the FSW joint, due to the lower heat conduction of this backing plate. The resulting microstructure is more homogeneous through the entire weld nugget.
- Only the stainless steel backing plate welds keep the fine as-welded grains unchanged after SHT. Secondary recrystallization and abnormal grain growth are leading to the coarsening of the other backing plate samples microstructures, up to mm scale grains.
- Measurements performed on various SHT tends to prove that secondary recrystallization is related to temperature, hardening phases, initial grain size and grain boundary stability. Higher temperatures leads to further recrystallization, while coarsening take place with dissolution of fine pinning η precipitates.
- The most important parameter is initial microstructure. None of the SHT conditions can avoid coarsening or AGG if the initial grains are smaller than a 2.5 µm threshold. Smaller 1 µm grains were also detected close to the coarse recrystallized grains. Stable grains present high angle grain boundaries as well as higher boundary energy, preventing them to grow under SHT.
- Preventing secondary recrystallization, either normal or abnormal grain growth, is then beneficial for mechanical performances. Excellent welds are produced with the stainless steel backing plate. A 100 % weld efficiency compared to the T6 state conditions and high ductility were reached in both longitudinal and transverse directions.

Acknowledgments

This research work has been supported by the European Research Council (ERC) under the European Union’s Horizon 2020 research and innovation program (grant agreement n716678).

M.B.L. acknowledges the support of the Fonds de la recherche scientifique - FNRS (FRIA grant), Belgium.

Pascal Jacques is acknowledged for EBSD and technical staff for manufacturing and support in sample testing.

Bibliography

[1] Tomoya Aoba, Masakazu Kobayashi, Hiromi Miura, Effects of aging on mechanical properties and microstructure of multidirectionally forged 7075 aluminum alloy, Materials Science and Engineering A 700, (2017) 220-225.

[2] Paul A. Rometsch, Yong Zhang, Steven Knight, Heat treatment of 7xxx series aluminium alloys - Some recent developments, Trans. Nonferrous Met. Soc. China 24, (2014) 2003-2017.

[3] Gerard M. Ludtka and David E. Laughlin, The Influence of Microstructure and Strength on the Fracture Mode and Toughness of 7XXX Series Aluminum Alloys, Metallurgical Transactions A, Volume 13A, (March 1982) 411-425.

[4] R.S. Mishra, Z.Y. Ma, Friction stir welding and processing, Materials Science and Engineering R 50, (2005) 1-78.

[5] Xing Huang, Qinglin Pan, Bo Li, Zhiming Liu, Zhiqi Huang, Zhimin Yin, Effect of minor Sc on microstructure and mechanical properties of Al-Zn-Mg-Zr alloy metal-inert gas welds, Journal of Alloys and Compounds 629, (2015) 197-207.

[6] W.M. Thomas, E.D. Nicholas, S.D. Smith, S.K. Das, J.G. Kaufman, T.J. Lienert, Aluminum 2001 - Proceedings of the TMS 2001 Aluminum Automotive and Joining Sessions, TMS, (2001) 213-224.

[7] RS Mishra, M Komarasamy, Friction stir welding of high strength 7XXX aluminum alloys, Elsevier (2016).

[8] A. Heidarzadeh, S. Mironov, R. Kaibyshev, G. Çam, A. Simar, A. Gerlich, F. Khodabakhshi, A. Mostafaei, D.P. Field, J.D. Robson, A. Deschamps, P.J. Withers, Friction stir welding/processing of metals and alloys: A comprehensive review on microstructural evolution, Progress in Materials Science.

[9] Z.Y. Ma, R.S. Mishra, F.C. Liu, Superplastic behavior of micro-regions in two-pass friction stir processed 7075Al alloy, Materials Science and Engineering A 505, (2009) 70-78.

[10] J.-Q. Su, T.W. Nelson, R. Mishra, M. Mahoney, Microstructural investigation of friction stir welded 7050-T651 aluminium, Acta Materialia 51, (2003) 713-729.

[11] Wei-feng Xu, Jin-he Liu, Microstructure evolution along thickness in double-side friction stir welded 7085 Al alloy, Trans. Nonferrous Met. Soc. China 25, (2015) 3212-3222

[12] A.H. Feng, D.L. Chen, and Z.Y. MA, Microstructure and Cyclic Deformation Behavior of a Friction-Stir-Welded 7075 Al Alloy, Metallurgical and Materials Transactions A, volume 41a, (April 2010) 957-971.

[13] Y. Huang and F. J. Humphreys, Measurements of grain boundary mobility during recrystallization of a single-phase aluminium alloy, Acta mater. Vol. 47, No. 7, (1999). 2259-2268.

[14] N. Martinez, N. Kumar, R.S. Mishra, K.J. Doherty, Effect of tool dimensions and parameters on the microstructure of friction stir welded aluminum 7449 alloy of various thicknesses, Materials Science & Engineering A 684, (2017) 470-479.

[15] Z.Y. Ma, A.L. Pilchak, M.C. Juhas, and J.C. Williams, Microstructural refinement and property enhancement of cast light alloys via friction stir processing, Scripta Materialia 58, (2008) 361-366.

[16] Fei Zhang, Xuekuan Su, Ziyong Chen, Zuoren Nie, Effect of welding parameters on microstructure and mechanical properties of friction stir welded joints of a super high strength Al-Zn-Mg-Cu aluminum alloy, Materials and Design 67, (2015) 483-491.

[17] H.J. Liu, X.L. Feng, Effect of post-processing heat treatment on microstructure and microhardness of water-submerged friction stir processed 2219-T6 aluminum alloy, Materials and Design 47, (2013) 101-105.

[18] P. Sivaraj, D. Kanagarajan, V. Balasubramanian, Effect of post weld heat treatment on tensile properties and microstructure characteristics of friction stir welded armour grade AA7075-T651 aluminium alloy, Defence Technology 10, (2014) 1-8.

[19] Z.L. Hu, M.L. Dai, and Q. Pang, Influence of Welding Combined Plastic Forming on Microstructure Stability and Mechanical Properties of Friction Stir-Welded Al-Cu Alloy, Journal of Materials Engineering and Performance 27, (2018) 4036-4042.

[20] I. Charit and R.S. Mishra, Abnormal grain growth in friction stir processed alloys, Scripta Materialia 58, (2008) 367-371.

[21] Kh. A.A. Hassan, A.F. Norman, D.A. Price, P.B. Prangnell, Stability of nugget zone grain structures in high strength Al alloy friction stir welds during solution treatment, Acta Materialia 51, (2003) 1923-1936.

[22] S.V. Sajadifar, G. Moeini, E. Scharifi, C. Lauhoff, S. Böhm, and T. Niendorf, On the Effect of Quenching on Postweld Heat Treatment of Friction-Stir-Welded Aluminum 7075 Alloy, Journal of Materials Engineering and Performance Volume 28(8), (August 2019) 5255-5265.

[23] M.A.García-Bernal, R.S.Mishra, R.Verma, D.Hernández-Silva, Inhibition of abnormal grain growth during hot deformation behavior of friction stir processed 5083 Al alloys, Materials Science & Engineering A 636, (2015) 326-330.

[24] F.C. Liu, B.L. Xiao, K. Wang, Z.Y. Ma, Investigation of superplasticity in friction stir processed 2219Al alloy, Materials Science and Engineering A 527, (2010) 4191-4196.

[25] Yiwei Sun, Xiaolong Bai, Daniel Klenosky, Kevin Trumble, and David Johnson, A Study on Peripheral Grain Structure Evolution of an AA7050 Aluminum Alloy with a

Laboratory-Scale Extrusion Setup, Journal of Materials Engineering and Performance, Volume 28(8), (August 2019) 5156-5164.

[26] Marie-Noëlle Avettand-Fenoel and Roland Taillard, Heterogeneity of the Nugget Microstructure in a Thick 2050 Al Friction-Stirred Weld, Metallurgical and Materials Transactions A, Volume 46a, (January 2015) 300-314.

[27] C.G. Rhodes, M.W. Mahoney, W.H. Bingel, M. Calabrese, Fine-grain evolution in friction-stir processed 7050 aluminum, Scripta Materialia 48, (2003) 1451-1455.

[28] F.J. Humphreys, M. Hatherly, Grain growth following recrystallization, in book: Recrystallization and Related Annealing Phenomena, (2004) 333-378.

[29] S Mironov and R Kaibyshev, Abnormal grain growth in fine-grained aluminum produced by friction-stir welding, IOP Conference Series: Material Science and Engineering 672, 012043, (2019) 1-4.

[30] J.-C. Ehrstrom, T. Warner, Brevet Constellium, Manufacturing method for friction welding aluminium alloys parts, Patent Application Publication, US 2005/0011932 A1, Jan 2005.

[31] S. Jana, R.S. Mishra, J.A. Baumann, G. Grant, Effect of process parameters on abnormal grain growth during friction stir processing of a cast Al alloy, Materials Science and Engineering A 528, (2010) 189-199.

[32] O.V. Gendelman, M. Shapiro, Y. Estrin, R.J. Hellmig, S. Lekhtmakher, Grain size distribution and heat conductivity of copper processed by equal channel angular pressing, Materials Science and Engineering: A, Volume 434, (2006) 88-94.

[33] M. J. Peet, H. S. Hasan and H. K. D. H. Bhadeshia, Prediction of thermal conductivity of steel, International Journal of heat and mass transfer, Vol. 54, (2011) 2602-2608.

[34] M. J. Assael and K. Gialou, Measurement of the Thermal Conductivity of Stainless Steel AISI 304L up to 550 K, International Journal of Thermophysics, Vol. 24, No. 4, (July 2003) 1145-1153.

[35] A. Simar, Y. Bréchet, B. de Meester, A. Denquin, T. Pardoen, Microstructure, local and global mechanical properties of friction stir welds in aluminium alloy 6005A-T6, Materials Science and Engineering A 486, (2008) 85-95.

[36] N. Kamp, A. Sullivan, R. Tomasi, J.D. Robson, Modelling of heterogeneous precipitate distribution evolution during friction stir welding process, Acta Materialia 54, (2006) 2003-2014.

[37] Christian B. Fuller, Murray W. Mahoney, Mike Calabrese, Leanna Micona, Evolution of microstructure and mechanical properties in naturally aged 7050 and 7075 Al friction stir welds, Materials Science and Engineering A 527, (2010) 2233-2240.

Supplementary material

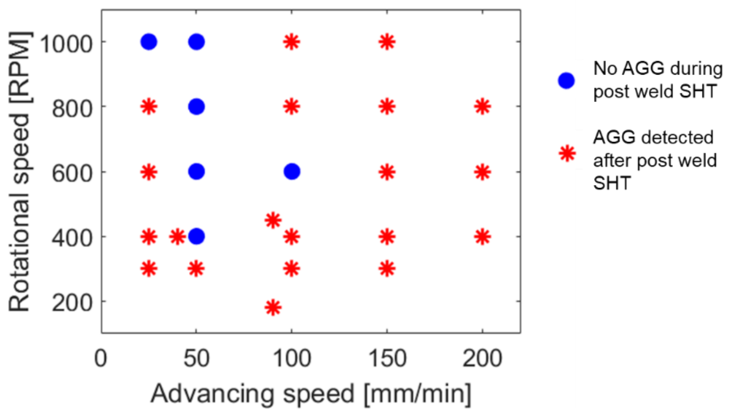

Figure S1: AGG occurrence in 7XXX alloys depending on welding parameters according to Charit et al *[20] and Hassan* et al *[21].*

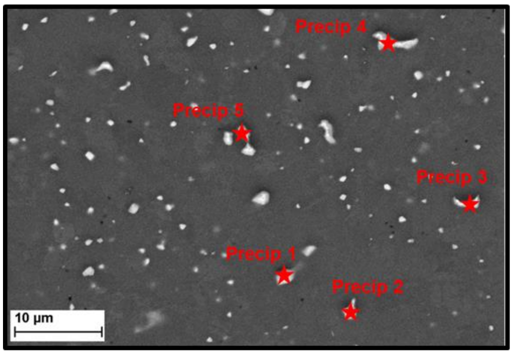

Spectrum	Al	Mg	Cu	Zn	Cr
Norm. mass percent (%)					
Al matrix	92,02	2,48	0,65	4,71	0,13
Precip. 1	43,53	13,54	40,20	2,59	0,14
Precip. 2	53,54	12,59	31,15	2,50	0,20
Precip. 3	62,19	9,88	24,54	3,13	0,25
Precip. 4	51,61	12,93	33,11	2,09	0,18
Precip. 5	52,36	10,71	34,01	2,67	0,21
Mean value:	52,65	11,93	32,60	2,60	0,20
Std deviation:	4,18	1,31	3,81	0,24	0,03

Figure S2: EDX evaluation of coarse precipitates. Rich in Cu, Mg, Al, probably S phase according to Liu et al. *[17].*